JOURNAL OF GEOPHYSICAL RESEARCH, VOL. 113, B12408, doi:10.1029/2007JB005314, 2008

Composition, microstructures, and petrophysics of the Mozumi fault, Japan: In situ analyses of fault zone properties and structure in sedimentary rocks from shallow crustal levels

Angela J. Isaacs,[1,2] James P. Evans,[1] Peter T. Kolesar,[1] and Tsuyoshi Nohara[3]

Received 20 July 2007; revised 13 August 2008; accepted 17 September 2008; published 18 December 2008.

[1] We characterize the chemical, microstructural, and geophysical properties of fault-related rock samples from the 80–100 m wide Mozumi fault zone, north central Honshu, Japan. The fault is exposed in a research tunnel 300–400 m below the ground, and we combine geological data with borehole geophysical logs to determine the elastic and seismic properties of the fault zone. Detailed mapping within the tunnel reveals that the fault zone consists of two zones of breccia to foliated cataclasites 20 and 50 m thick. Two narrow (tens of centimeters wide) principal slip zones on which most of the slip occurred bound the central fault zone. The dominant deformation mechanisms within the fault zone were brittle fracture, brecciation, slip localization, plastic deformation, and vein formation in a sericite-calcite rich matrix. Clay alteration patterns are complex within the fault zone, with clay-rich fault breccia enriched in smectite, illite, and kaolinite relative to the kaolinite and illite dominant in the host rock. Whole rock geochemical analyses show that the fault-related rocks are depleted in Fe, Na, K, Al, Mg, and Si relative to the host rock. The fault zone exhibits depressed electrical resistivity values by 10–100 ohm m relative to the wall rock, values of V_p and V_s values that are ~0.30 and ~0.40 km/s (10–20%) less than protolith values. The spontaneous potential logs indicate that the fault zone has increased freshwater content relative to formation waters. Wellbore-based measurements of V_p and V_s in fault-related rocks to enable us to calculate values of Young's modulus from 16.2 to 44.9 GPa and Poisson's ratio for the fault zone of 0.263 to 0.393. The protolith has Young's modulus of 55.4 GPa and a Poisson's ratio of 0.242. Lowest calculated values of Young's modulus and highest calculated values of Poisson's ratio correspond to fault breccia with increased porosity, high fluid content, and low resistivity values. Taken together, these data show that the shallow portion of the Mozumi fault consists of a complex zone of anastomosing narrow slip zones that bound broad zones of damage. Fluid-rock alteration and deformation created altered fault-related rocks, which have resulted in overall reduced interval velocities of the fault zone. These data indicate that seismic waves traveling along the interface or internally reflected in the fault zone would encounter rocks of differing and reduced elastic properties relative to the host rocks but that in detail, material properties within the fault may vary.

Citation: Isaacs, A. J., J. P. Evans, P. T. Kolesar, and T. Nohara (2008), Composition, microstructures, and petrophysics of the Mozumi fault, Japan: In situ analyses of fault zone properties and structure in sedimentary rocks from shallow crustal levels, *J. Geophys. Res.*, *113*, B12408, doi:10.1029/2007JB005314.

1. Introduction

[2] As structural geologists who study fault zone structure and composition, we are often asked by geophysicists questions such as the following: What are fault zones seismically? How can we represent their velocity structure? What are the resistivity or conductivity properties of faults? Likewise, hydrogeologists ask what is the permeability of a fault? These simple questions belie the fact that determining the composition and structure of fault zones at all levels of the crust is an important element in understanding a variety of deformation and fluid flow processes in the crust, including how faults affect fluid flow, how slip and damage is distributed within a fault, and how seismic energy is distributed during an earthquake. Addressing the questions posed above requires that we determine physical properties of fault-related rocks, and determine how these properties came to be.

[1] Department of Geology, Utah State University, Logan, Utah, USA.
[2] Now at Anadarko Petroleum Corporation, Denver, Colorado, USA.
[3] Geological Isolation Research Project, Neotectonics Research Group, Japan Atomic Energy Agency, Gifu, Japan.

0148-0227/08/2007JB005314$09.00

[3] One popular model of fault zone structure is the "Chester model" [*Chester and Logan*, 1986; *Chester et al.*, 1993] in which a fault is represented as a core of highly sheared rock, embedded within a damage zone of fractured and faulted rock. *Caine et al.* [1996] suggest that fault zone structure may vary from very narrow faults with little associated damage to a wide zone of deformation with little or no slip localization. Most faults are a combination of a very narrow zone of concentrated slip, termed the principal slip surface (PSS), which is surrounded by a damage zone that is much thicker than the fault core and is characterized by high densities of subsidiary faults, fractures, and veins. The damage zone is interpreted as recording deformation over much of the history of the fault [*Chester and Logan*, 1986; *Schulz and Evans*, 2000; *Chester et al.*, 2004] and in faulted crystalline rocks, the damage zone is often a zone of higher permeability and porosity relative to the protolith [*Evans et al.*, 1997; *Wibberley and Shimamoto*, 2003]. The proportions of each component may vary along and between faults, with some faults exhibiting little in the way of a damage zone.

[4] While appropriate for a class of faults, the Chester model should likely be modified for other types of faults. In fine-grained sedimentary rocks for example, significant deviations from the Chester fault model zone may occur [*Erickson*, 1994; *Warr and Cox*, 2001; *Yan et al.*, 2001; *Heermance et al.*, 2003; *Holland et al.*, 2006; *Faulkner et al.*, 2003]. Faults in phyllosilicate-rich and clay-rich rocks [*Rutter et al.*, 1986; *Keller et al.*, 1995] may exhibit thick broad zones of damaged rock, punctuated by an anastamozing network of gouge zones. Slip is interpreted to be accommodated on numerous narrow slip zones that lie within the broad zone of deformation.

[5] In addition to geological studies, fault zone properties and structure can be investigated with a variety of inversion methods of fault zone waves [*Ben-Zion*, 1998; *Ben-Zion and Sammis*, 2003; *Li et al.*, 1999, 2004; *McGuire and Ben-Zion*, 2005]. The temporal variations in fault zone properties can examine fault healing [*Li et al.*, 2003], and analyses of fault zone properties contribute to evaluating earthquake hazards along fault zones [*Spudich and Olsen*, 2001]. Geologic observations can be merged with geophysical studies of fault zone structure and composition to help constrain the properties of the fault zone over a range of scales [*Blakeslee et al.*, 1989; *Gettemy et al.*, 2004] that in turn can be used to examine the seismological structure of a fault and its impact on propagation of seismic waves. Many of the physical properties within fault zones at in situ conditions are difficult to resolve, but are critical for evaluating fault zone processes, such as the transmission and internal reflection of seismic energy [*Spudich and Olsen*, 2001; *Gettemy et al.*, 2004] and the distribution of and frequency content of seismic energy that may travel within a fault zone [*Li and Vidale*, 1996]. Direct measurement of elastic and seismic properties is difficult, owning to the friable nature of many fault-related rocks in the field and the difficulty of drilling into and retrieving samples from core. *Gettemy et al.* [2004] used P wave seismic methods to infer the structure and petrophysical properties of an exposed fault zone, and showed that the internal structure of large strike slip faults can be complex, with regions of low seismic velocity and high anisotropy. Estimates of the seismic velocity contrasts across faults, using a variety of inversion schemes, range from 5% to more than 30%, depending on the location, depth, and resolution of the imaging method [*Eberhart-Phillips and Michael*, 1998; *McGuire and Ben-Zion*, 2005; *Thurber et al.*, 2006; *Hardebeck et al.*, 2007]. The question we pose here is what are the material properties of fault zone materials measured in situ, what are the processes that might cause these material property variations, and what are the textures in the rocks produced by these processes?

[6] In order to evaluate the in situ petrophysical properties and near-surface structure of a fault zone, we present results of a study of the composition, structure, physical properties, textures, and fluid-rock interactions of rocks from a fault zone sampled at ~400 m below the ground surface in western Japan. Rock samples from drilled core associated with the Active Fault Survey Tunnel (AFST) and continuous borehole geophysical logs are combined with data on porosity and permeability to document the variations in fault zone properties across the fault. We discuss the results in light of a recent study of inversion of fault zone waves in the Mozumi fault [*Mamada et al.*, 2004; *Mizuno et al.*, 2004] and in situ hydraulic tests [*Nohara et al.*, 2006] to document the relationship between deformation mechanisms, alteration, and elastic properties of the fault zone. This work provides data on the in situ chemical, physical, and mechanical properties of the internal portion of an active fault in clastic sedimentary rocks in the upper portion of the crust, but at depths where weathering has not disturbed the textures and structures associated with faulting and fluid flow. The AFST also provides exposures of a fault at depths where seismic energy is transmitted to the surface, but above the region in which seismic energy is radiated. Analysis of the Mozumi fault zone exposed in the Active Fault Survey Tunnel provides a unique opportunity to merge geochemical, mineralogic, and petrophysical studies of fault-related rocks (this study) with results of hydrologic properties testing [*Forster et al.*, 2003] and fault zone guide wave studies [*Mizuno et al.*, 2004] to determine the nature of the fault zone scale variability of petrophysical properties and their causes.

1.1. Geologic Setting

[7] The Mozumi fault (MF) is a northeast striking, right-lateral strike-slip fault in north central Japan with 125–500 m of slip (Figure 1) [*Ando*, 1998]. The research tunnel excavated by the Terrestrial Subsurface in Earthquake Frontier Project at ~300–400 m below the surface trace of the fault intersected the Mozumi fault to provide direct access and observation of this active, clay-rich fault zone over 200 m across the fault zone and host rocks (Figure 2). The Mozumi fault zone is 80–100 m wide and is an example of a complex, heterogeneous fault zone in sedimentary rocks [*Mamada et al.*, 2002, 2004; *Forster et al.*, 2003; *Mizuno et al.*, 2004; *Nohara et al.*, 2006]. In addition to the tunnel, samples were acquired from horizontal and 60° plunging boreholes that crossed the entire fault zone.

[8] The general geology of the region is summarized by *Kawai and Nozawa* [1958], *Soma and Akiyama* [1984], and *Yamada et al.* [1989].The Mozumi fault is 23 km long, branches northwest from the southeastern end of the Atotsugawa fault [*Ando*, 1998; *Takeuchi et al.*, 2003], strikes ~N 50–60°E and has a near-vertical dip [*Hirahara et al.*,

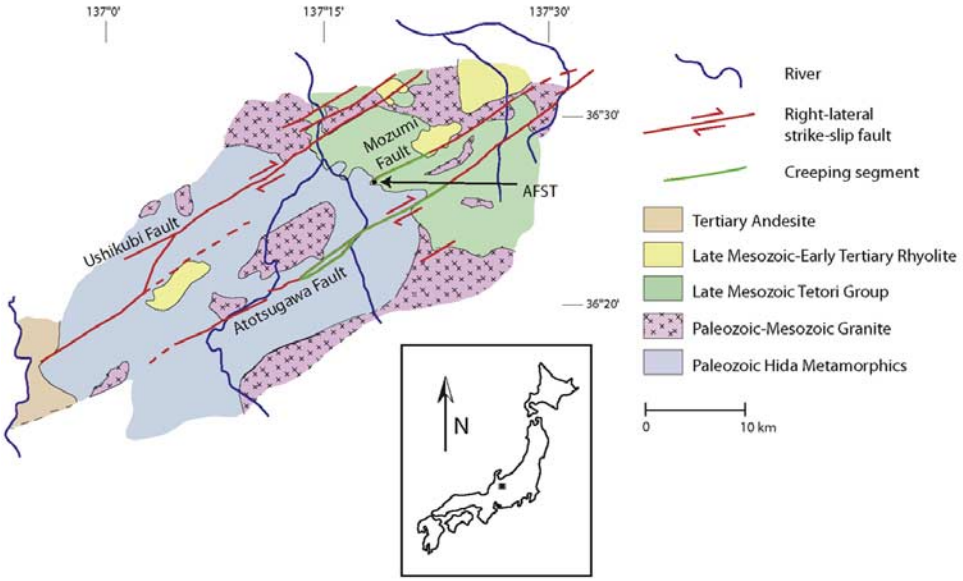

Figure 1. Generalized geology surrounding the Atotsugawa, Mozumi, and Ushikubi faults, Japan (Atotsugawa Fault System). The Active Fault Survey Tunnel (AFST) intersects the Mozumi fault where it cuts Jurassic-Cretaceous Tetori Group sandstone and shale (map modified from *Matsuda* [1966]). Inset map shows the location of the area.

2003; *Takeuchi et al.*, 2003]. In the study area, the fault strikes ~N 40–45°E nearer the northwest termination of the Mozumi fault, where the fault appears to bend [*Ito*, 1999; *Mizuno et al.*, 2004].

[9] The Mozumi fault has an earthquake recurrence of 13,500 ± 6,300 years [*Takeuchi et al.*, 2003]. The central part of the Mozumi fault creeps [*Ito*, 1999, 2003; *Hirahara et al.*, 2003], whereas the northeastern and southwestern portions of the fault system appear to be locked, as indicated by the distribution of intense microseismicity [*Ito*, 1999, 2003]. Creep on the fault system is supported by geodetic measurements and boreholes strainmeters [*Ito*, 1999, 2003]. Modeling by *Hirahara et al.* [2003] indicates that the creep rate in the central segment is 1.5 mm/a, and that creep extends from the surface to ~7 km depth. Low levels of seismicity occur along the northwestern and central sections of the Mozumi fault and the central section of the Atotsugawa fault [*Mikumo et al.*, 1988; *Wada et al.*, 1990].

1.2. Active Fault Survey Tunnel

[10] The Active Fault Survey Tunnel (AFST) project in Gifu prefecture, Japan, trends N 24°W for 481 m from an access point from a tunnel in the Kamioka Pb-Zn-Ag deposit [*Mariko et al.*, 1996]. The tunnel provided direct access of the Mozumi fault at a depth of 300–400 m (Figure 2) [*Shingu et al.*, 1997]. Within the fault survey tunnel, the Mozumi fault cuts sandstone, shale, and siltstone of the middle Jurassic to lower Cretaceous Tetori Group (Figure 2) [see also *Matsuda*, 1966]. The Tetori Group overlies Paleozoic Hida metamorphic rocks and Paleozoic-Mesozoic granite in the area. The Tetori Group consists of alternating conglomerate, fine to very coarse-grained sandstone, shale, siltstone, and coal seams [*Fujita*, 2002]. These sedimentary rocks are also overlain by the Hida Gneiss along the Yokoyama thrust.

[11] The AFST was mapped by geologists of the Mitsui Mining and Smelting Co. as part of the development of the tunnel for scientific research (Figure 2) [*Forster et al.*, 2003; *Nohara et al.*, 2006]. The map in Figure 2 is derived directly from the unpublished mine geologists data. Mine mapping along the tunnel before it was lined revealed the presence of two damage zones, termed "crush zones" by the mine geologists. Zone A is ~20 m wide and is interpreted as the main trace of the Mozumi fault, and crush zone B is ~65 m wide and is interpreted as a subsidiary fault to the Mozumi fault [*Forster et al.*, 2003]. Hereafter, crush zone A is referred to as the Mozumi fault or primary damage zone. Adjacent to the damage zones lie narrow clay-rich slip zones that appear to be 10–20 cm wide. Only one of these zones was exposed during our work, but descriptions of these zones, translated from the Japanese report [*Shingu et al.*, 1997], indicates that the fault zones are characterized by clay gouge and fault breccia. The mine map also documents the presence of six thin fault zones, which are interpreted to be the loci of most of the slip within the fault zone [*Nohara et al.*, 2006].

2. Characterization of Mozumi Fault Rocks

[12] Except for a small window through the AFST lining, the only direct access to the fault-related rocks is in four cored and logged boreholes drilled off of the main tunnel (Figure 2). Borehole 1 was horizontal and intersected the largest subsidiary fault (zone B). Boreholes A and 2 intersect the main trace of the Mozumi fault, and borehole A plunged 60° north-northwest from the horizontal Active Fault Survey Tunnel. Borehole 3 samples lithology outside of the fault zones northwest of the fault. Unoriented core samples of siltstone were collected from borehole A of the Active Fault Survey Tunnel (samples MZA-1 through

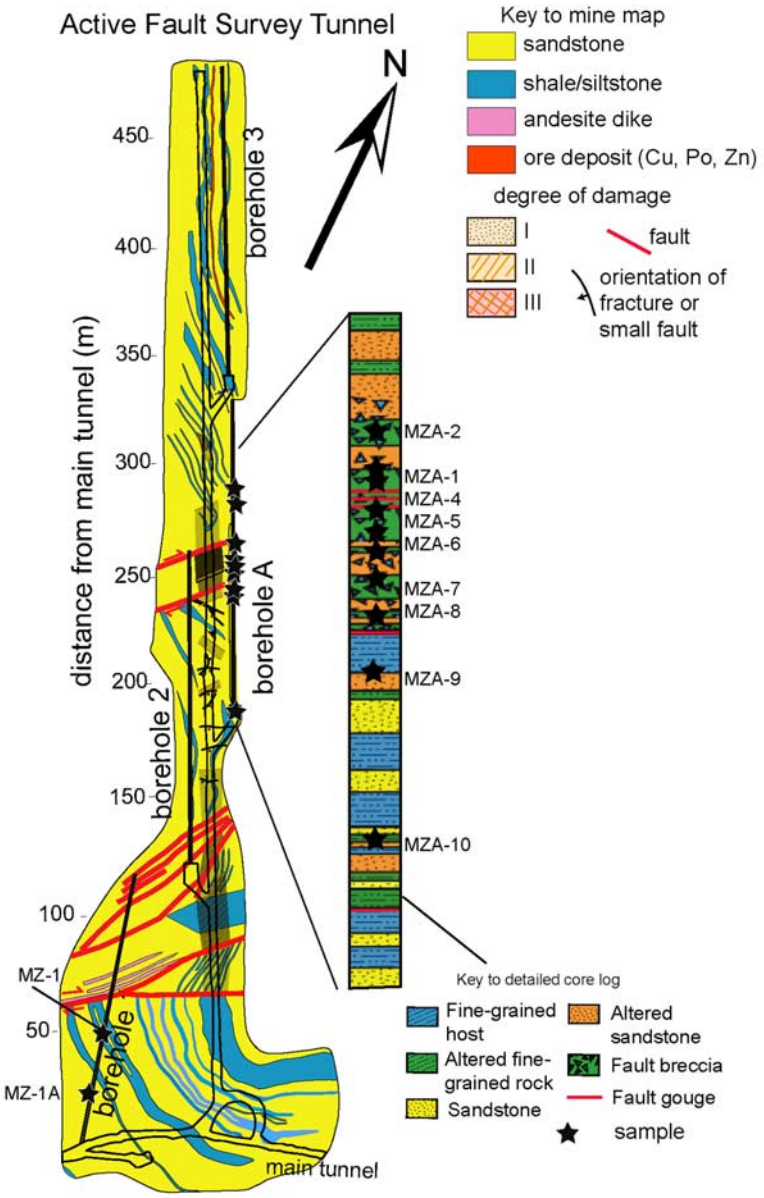

Figure 2. Geologic map of the Active Fault Survey Tunnel and detailed core log from borehole A. This map is extracted from a 1:500 map created by geologists of the Mitsui Mining and Smelting Company in 1997 along the tunnel walls and supplemented by core logs of the boreholes. Lithologies and structures are shown as described by the mine geologists. Borehole A is inclined 60° to N24° west, and sample locations and lithology within the box have been projected to the horizontal. Samples discussed in this study are from borehole A. All samples collected in borehole A are siltstone. Sample MZ-1, collected from borehole 1, is siltstone protolith. Data from boreholes 1 and 2, shown in Figure 4, cut both of the major fault zones. The lithologic log is an expansion of the region sampled across the main portion of the fault zone, and the stratigraphy is expanded. The map presents the data from mine geologists; the stratigraphic log is based on detailed observations of the core.

MZA-10; Table 1). Three samples of undeformed medium-grained sandstone (MZ 1A) were collected from 26.9 m along borehole, and two siltstone samples (MZ-1) was collected 50.1 m from the southwest end of borehole 1. These samples are similar to the clasts of siltstone breccia in the fault zone, has similar bulk mineralogy, and are used to compare both the microstructures and geochemistry to samples from the Mozumi fault zone. We also use the mine mapping of the fault to evaluate the mesoscopic structure of the fault and host rock.

2.1. Fractures and Rock Quality

[13] Map-scale and mesoscopic structural data of borehole A were provided by Power Reactor and Nuclear Fuel Development Corporation (now Japan Atomic EnergyAgency)

Table 1. Descriptions of Samples From the Mozumi Fault Zone Used in This Study Including Distances Along the Borehole and Projected Horizontal Distances From the Southeast End of Borehole A

Sample	Description	Distance Along Borehole (m)	Horizontal Distance (m)
MZA-2	Siltstone fault breccia, abundant clay, intensely foliated matrix and shear fabric	143.2	71.6
MZA-1	Siltstone fault breccia, abundant clay, crenulation foliation in matrix, hematite and debris-filled fractures	133	66.5
MZA-4	Siltstone fault breccia, abundant clay, calcite and quartz veins, intensely foliated matrix	128.4	64.2
MZA-5	Siltstone fault breccia, abundant clay, intensely foliated matrix and shear fabric	122.4	61.2
MZA-6	Siltstone fault breccia, moderately foliated, shear fabrics	116.57	58.3
MZA-7	Siltstone fault breccia, abundant clay, intensely foliated matrix and shear fabric	111.76	55.9
MZA-8	Siltstone, angular fault breccia, calcite veins, fractures, anastomosing brown clay	104.8	52.4
MZA-9	Altered siltstone cut by subsidiary fault, indurated and mineralized siltstone against weak clay-rich fault rock	95.75	47.9
MZA-10	Siltstone, fault with clay gouge, quartz and calcite veins	38.2	19.1

from a report [*Shingu et al.*, 1997]. Orientations of fractures in borehole A (Figure 3) were measured for wall rock and Mozumi fault rock; however, few fractures were measured within the Mozumi fault zone because the rocks are brecciated, resulting in a small number of recognizable discrete fractures. Three main sets of fractures are seen (Figure 3): Fracture set 1 has a mean orientation of 155°, 20° and is at a mean angle of 82° to the main trace of the fault. Two nearly vertical subsidiary fracture sets are oblique to the Mozumi fault: one with a mean orientation of 001°, 71° that makes a 42° angle with Mozumi fault (fracture set 2), and the other with a mean orientation of 063°, 74° that makes a 28° angle with the Mozumi fault (fracture set 3).

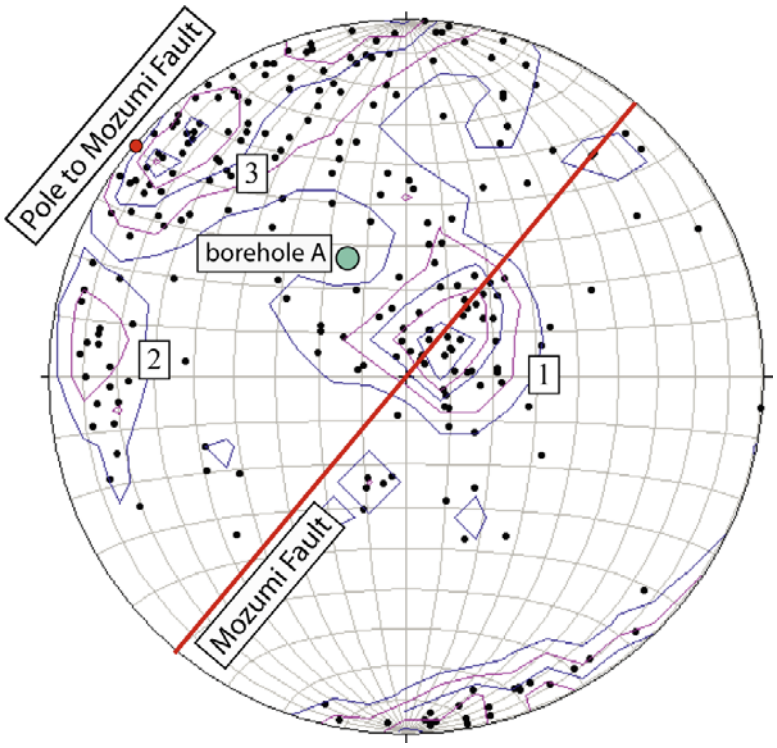

Figure 3. Lower hemisphere equal-area stereonet of contoured poles to fracture planes recorded along borehole A of the Active Fault Survey Tunnel (data presented in tables of *Shingu et al.* [1997]). The orientation of borehole A and the Mozumi fault within the Active Fault Survey Tunnel are also shown for reference. Fracture set 1 has a mean orientation of 155°, 20° west. Fracture set 2 has a mean orientation of 001°, 71° east. Fracture set 3 has a mean orientation of 063°, 74° south.

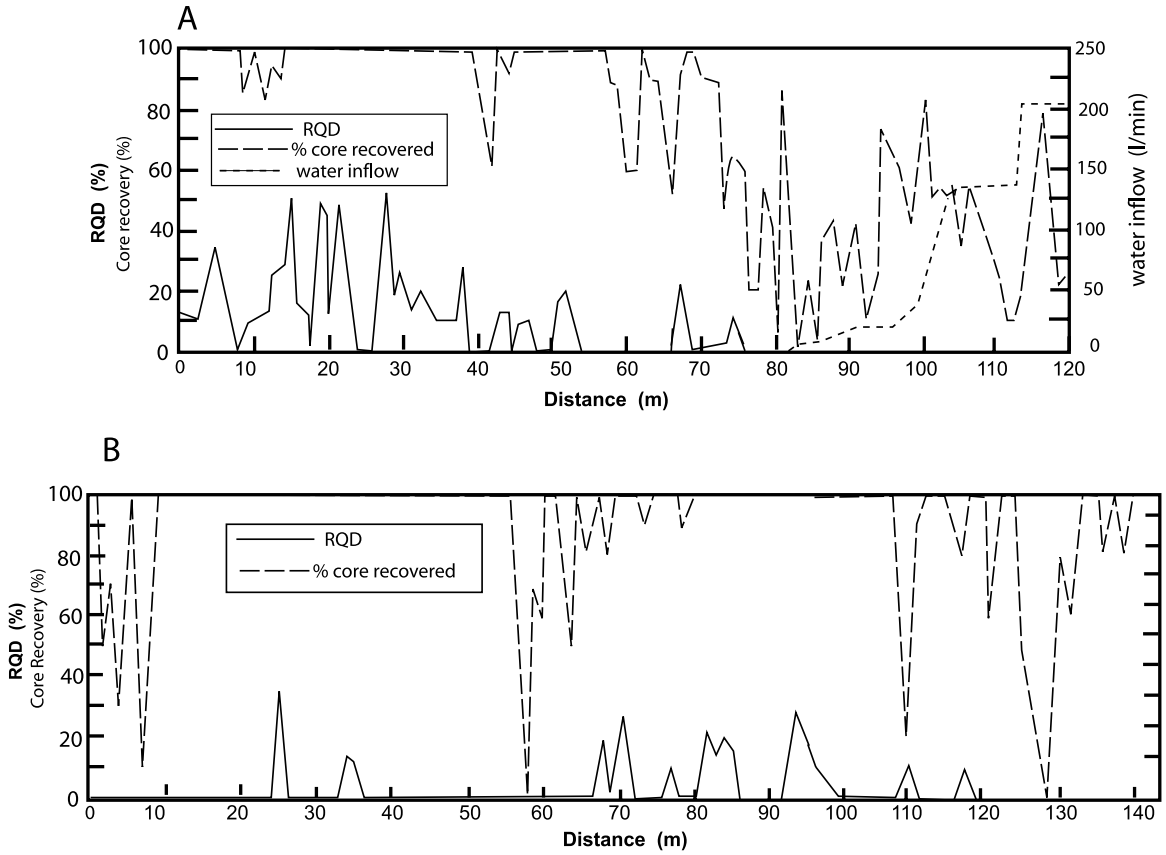

Figure 4. Rock quality descriptor (RQD) and core recovery for boreoles 1 and 2. (a) Borehole 1 crosses the southern fault strand and incorporates a zone of intact rock next to a region of highly fractured rocks in the fault. (b) Data for borehole 2 which crosses the zone interpreted to be the main fault zone. RQD, core recovery, and water fluxes mark the fault zone.

[14] Mine geologists recorded the Rock Quality Designation (RQD), core recovery, and water inflow along the cored intervals for several of the boreholes that crossed the faults (Figure 4). The RQD scheme is a measure of rock integrity, which is defined as the percentage of core pieces in a given length of core that are twice the core diameter [*Deere and Deere*, 1987]. The rock quality indices of rock masses surrounding the Mozumi fault range from 0 to 60%. A value of <25% indicates very poor rock quality, 25–50% indicates poor rock quality and 50–75% indicates fair rock quality. Rock quality is reported as 0–10% across the "crush zones" of the Mozumi fault, reflecting a high degree of mesoscopic damage as determined by the mining geologists. Core recovery reflects the quality of the faulted rock, and significant fluxes of water were recorded at the main fault zone (Figure 4a).

2.2. Core Samples and Microstructures

[15] The undeformed Tetori Group rocks are a sequence of very fine to fine-grained siltstone and fine- to coarse-grained sandstones with subrounded quartz grains in the fine-grained matrix (Figures 5a, 6a, and 6b). The fine-grained portions of the siltstone protolith are thinly to medium bedded, and little deformation can be seen surrounding larger quartz grains. There are relatively few clay mineral grains in the siltstone (Figures 6a and 6b). The sandstone sequence consists of fine- to coarse-grained, subangular to subrounded quartz and feldspar sandstones and arkoses. Microstructures of deformed rocks from a secondary fault in borehole A consist of siltstone cut by several veins and narrow faults containing clay films (Figure 5b). The siltstone has a sericite-rich matrix, as well as calcite and phyllosilicates. Veins consist of fine-grained quartz at fracture walls that progressively coarsens inward and surrounds a central and final phase of calcite vein fill (Figure 6c).

[16] The southeast edge of the fault zone consists of altered siltstone cut by a fault of unknown size (Figure 7). In hand sample, the fault makes a clear separation of heavily altered, indurated siltstone and highly comminuted clay-rich fault rock. The fault interface is smeared with tacky, green, chlorite-rich clay. Twinned calcite grains (Figure 6d) indicate plastic deformation and appear to have been injected into the rock because they are found in irregularly shaped, discontinuous zones that have sharp boundaries with surrounding quartz grains. Approaching the fault, quartz grain size decreases, and additional mineral phases are present. Calcite is present nearest the fault, bordered by a zone of quartz and chlorite, and less deformed quartz, calcite, and some feldspar are present. There are also radial growths of epidote (Figure 6e) and zoned quartz with styolite-like sutures (Figure 6f).

[17] Samples from the primary damage zone of the Mozumi fault (Figures 6c–6f) contain evidence for shearing

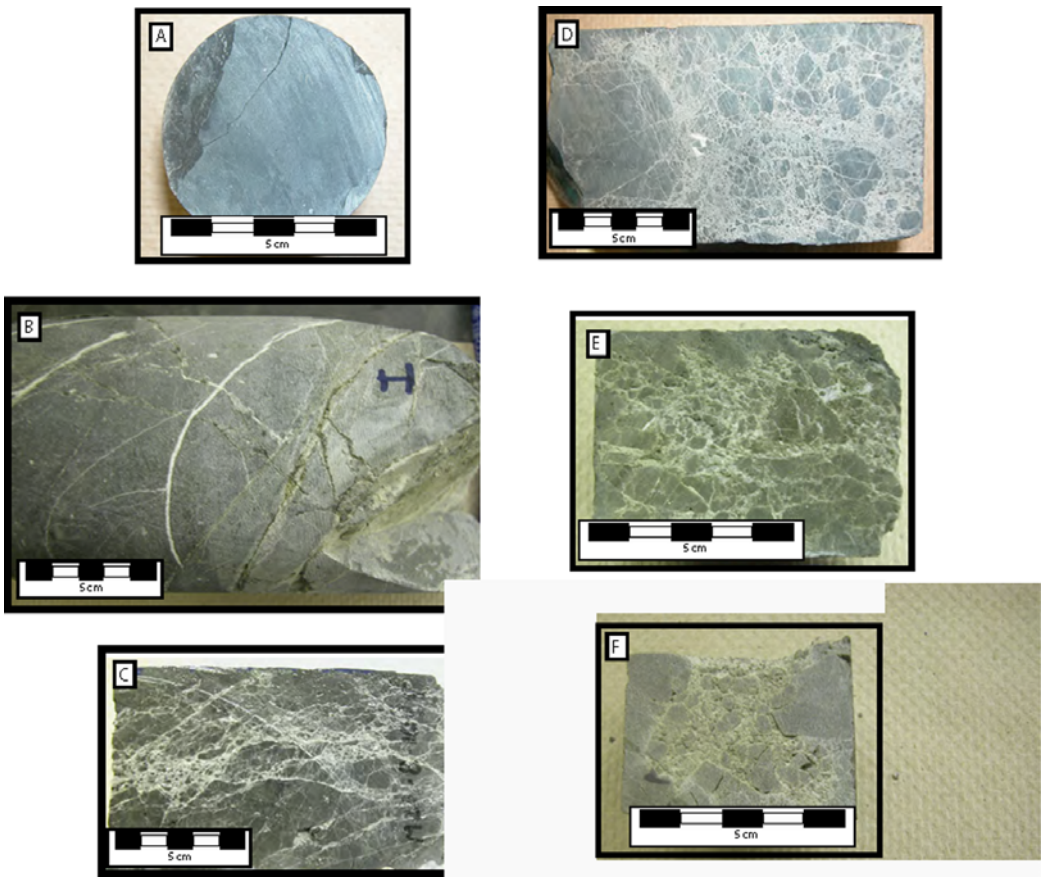

Figure 5. Photographs of cores samples from boreholes of the Active Fault Survey Tunnel. (a) MZ-1 (protolith), sample from borehole 1 of undeformed siltstone. (b) MZA-10, siltstone sample from borehole A collected from a subsidiary fault zone. (c) MZA-8, siltstone sample from the Mozumi fault zone within borehole A. The sample is wet, and fault breccia and surrounding clay fabric can be seen. (d) MZA-7, siltstone sample from the Mozumi fault zone in borehole A. Dry fault breccia sample with abundant clay. (e) MZA-5, siltstone sample from the Mozumi fault zone within borehole A; wet fault breccia. (f) MZA-1, siltstone fault breccia from the Mozumi fault zone within borehole A.

and brittle grain size reduction. Foliation of the sericite-rich matrix changes character and becomes more intense toward the core of the fault. Calcite veins are common, and fractures are partially filled with clasts ripped from the sidewalls. Discontinuous, anastomosing brown clay seams (Figures 6g and 6h) are randomly oriented in curving stringers which die out into the surrounding siltstone. Small injections of clay into the surrounding wall rock start at the shear zone and die out into the siltstone. Some of these bands have entrained portions of the matrix. Siltstone and clay bands are sometimes cut by chlorite veins that represent an additional fluid phase not recorded in quartz and calcite veins. Larger veins contain at least two mineral phases growing away from the fracture walls.

[18] Quartz grains range from undeformed to brecciated, shattered, cut by veins and microfractures. Quartz grains are also sometimes rimmed by calcite or other minerals, and have wavy to patchy extinction. Feldspar grains commonly show evidence for dissolution including irregular edges replaced by calcite. Large twinned calcite crystals and pyrite (Figure 6i) are also present. Subrounded and rotated porphyroclasts are present within the matrix material. Some porphryoclasts have open fractures (Figure 6j). Fault breccia and porphyroclasts sometimes contain pieces of quartz and calcite veins, or can be identified by foliation directions that differ from surrounding foliation (Figure 6k). Microfaults that offset clay bands, cut veins, and juxtapose foliations of different orientations are also common (Figure 6l). Fracture contain sidewall rip off clasts indicating movement (Figure 6m), and in many cases tip out into shear zones (Figure 6n). Overall, samples from the Mozumi fault display a strong foliation parallel to the Mozumi fault, and a weak foliation perpendicular to the Mozumi fault.

2.3. Composition

2.3.1. Bulk and Clay Mineralogy

[19] Bulk powder X-ray diffraction identifies quartz, feldspar, calcite, muscovite/illite, montmorillonite (smectite), kaolinite, and chlorite and/or vermiculite as the main mineral constituents in the samples. All samples contain illite/muscovite and kaolinite clays. Several samples from the primary damage zone contain smectite mixed with combinations of illite, kaolinite, and possibly chlorite or vermicullite (Table 2). Samples from the southeast edge of the primary damage zone as well as across the core of the fault contain smectitic clay mixed with illite/muscovite and

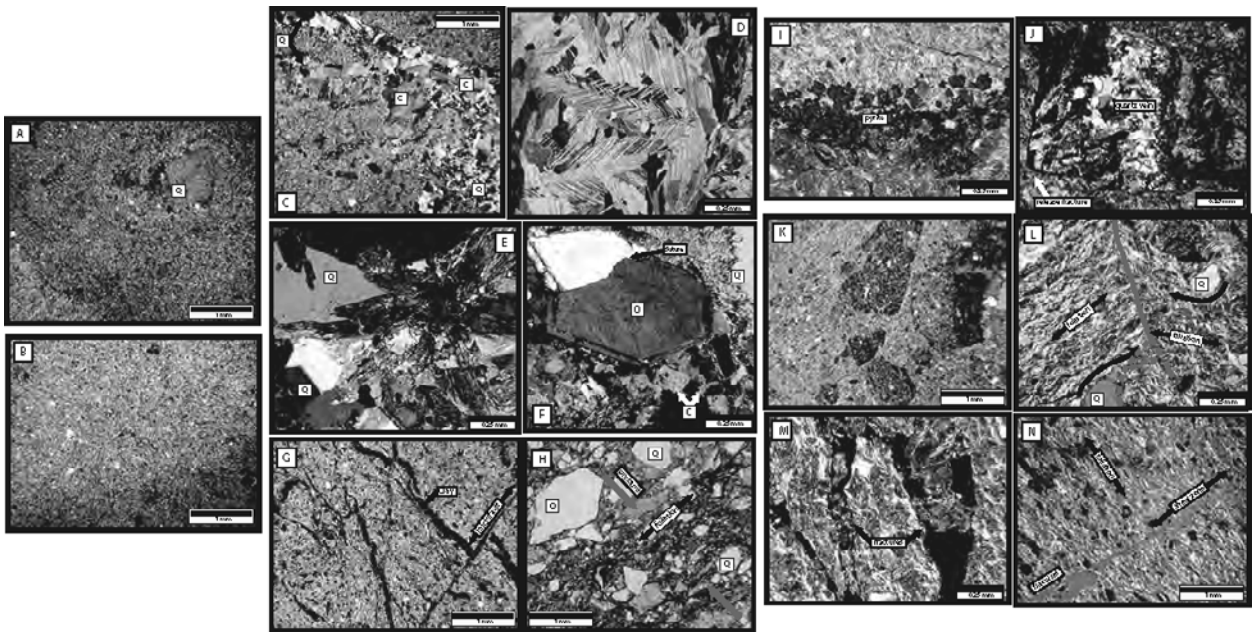

Figure 6. Photomicrographs of Mozumi fault zone samples and protolith. (a) MZ-1, siltstone protolith. No deformation is seen in fine-grained matrix surrounding large quartz crystal. (b) Ma-1: siltstone protolith. (c) MZA-10: evidence for evolving fluids. (d) MZA-9, plastically deformed calcite that may have been injected into surrounding rock. (e) MZA-9, radial growths of epidote. (f) MZA-9, zoned quartz grains with stylolites. (g) MZA-8, anastomosing clay. (h) MZA-7, foliated fault rocks. (i) MZA-5, pyrite crystals. (j) MZA-6, foliated fault rocks showing release fractures. (k) MZA-2, foliated fault rocks with rotated porphyroclasts of matrix and vein material. (l) MZA-1, crenulation foliation. (m) MZA-1, partially open fractures with debris sheared from surrounding walls. (n) MZA-1, fractures tip out into shear zones. Polarized light in Figures 6a, 6b, 6c, 6d, 6e, 6f, 6g, and 6j. Polarized light with 530 nm plate in Figures 6h and 6n. Plain light in Figures 6i and 6l. Reflected light in Figure 6k. Q, quartz; C, calcite.

kaolinite, and possibly small amounts of chlorite and R_0 I-S (disordered illite-smectite clay minerals). Samples from the northwest edge of the primary damage zone are composed of illite/muscovite and kaolinite. Chlorite or vermiculite and kaolinite-montmorillonite clays are present along the secondary fault at the northwest edge of the primary damage zone. The siltstone protolith contains illite/muscovite and kaolinite, and possibly a small amount of R_0 I-S. The relative amount of muscovite and illite in each sample is unknown, and these minerals have been considered as one mineral phase.

2.3.2. Chemical Composition

[20] Whole rock geochemical analyses of fault-related rocks provide a measure of the geochemical changes in the fault. Whole rock inductively coupled plasma mass spectrometry analysis was used to evaluate the geochemistry of the fault zone. We use the whole rock data to calculate volumetric change, after the method of *Goddard and Evans* [1995] in which the whole rock analyses in fault-related rocks are compared with protolith values. This allows us to estimate the degree of constituent loss or gain within the fault, relative to the protolith. The analyses show that the fault zone samples are depleted in Na, Al, Fe, Mg, Si, and K oxides relative to the protolith (Figure 8). The calcium values show that it is enriched for nearly all fault zone samples. The values of SiO_2, LOI (loss on ignition, a measure of volatile content), Fe_2O_3, and CaO are the most significant variables that change across the fault zone as determined by principal component analysis. Samples nearer the southeast and northwest edges of the primary damage zone are generally depleted with respect to the host rock, but less so than samples nearer the fault core. These data indicate fluid flow that facilitates the movement of oxides through the fault zone resulting in chemical changes in the fault rocks relative to the protolith. Fluid-rock interactions suggested by these geochemical changes indicate that significant amounts of the original rock volume in and around the fault zone were dissolved and replaced by Ca-bearing minerals.

3. Petrophysics of Fault-Related Rocks

3.1. Wireline Log Interpretations

[21] Six borehole geophysical logs were recorded for borehole A [*Shingu et al.*, 1997]. These logs have been projected to the horizontal (Figure 9) and were correlated to samples collected from borehole A for petrophysical analysis. These logs measure different physical responses and are useful in determining the bulk (1–10 m) properties of Mozumi fault rocks. The spontaneous potential (SP), natural gamma ray, and resistivity logs provide insights into the composition of the rocks, and the acoustic, sonic, and compressional and shear wave (V_p and V_s, respectively) logs provide direct measurement of the seismic properties. In addition, the ratio of the P wave velocity to the S wave velocity (V_p/V_s) is an indicator of the presence of fluids, with high values of V_p/V_s indicating high fluid content.

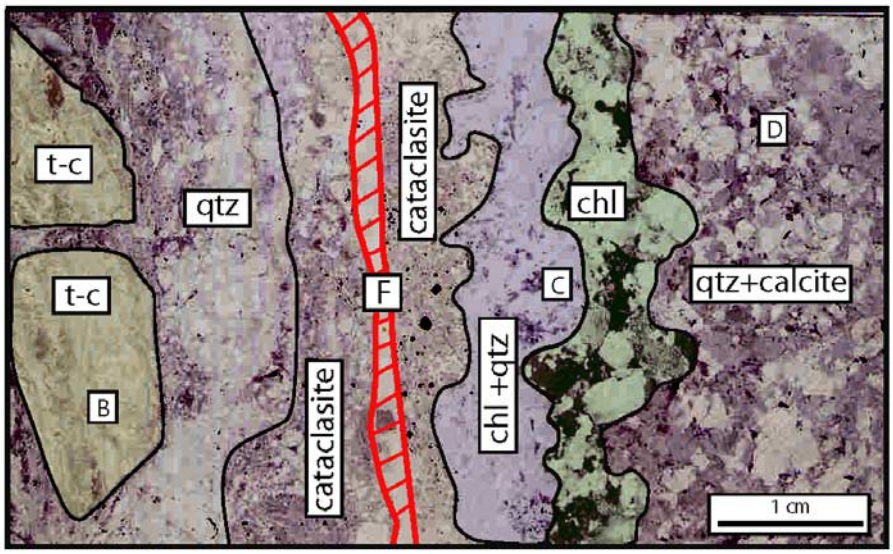

Figure 7. Photograph of thin section of sample MZA-9. Zones of different mineral phases have been outlined, shaded, and labeled. The sections labeled t-c are purely twinned calcite. Other zones are labeled by the dominant mineral; however, these zones are not pure. Multiple mineral phases along the fault provide evidence for fluid flow in and around the fault, and zones of twinned calcite crystals indicate fluid pressurization and injection. The locations of photomicrographs in Figures 6b, 6c, and 6d are indicated. Abbreviations: t-c, twinned calcite; qtz, quartz; chl, chlorite; F, fault.

[22] The wireline logs show that the fault zone has a variable signature, depending on the log examined. The most notable log signature associated with the fault zone is a reduction in the resistivity log (Figure 9). Rocks outside the fault zone have resistivities as high as 100 ohm m, whereas within the fault zone, resistivity decreases to nearly 0, likely indicating the presence of water in the fault zone. Rocks southeast of the fault zone also demonstrate a similar reduction in shaly rocks. The fault zone signature is also seen in the SP log, where an increase is observed over the protolith, and a modest reduction of V_p and V_s.

[23] The resistivity log records nearly the same response for long- and short-range curves. Low resistivity values (0–50 ohm m) indicating increased pore fluids are recorded across the Mozumi fault. A deflection from the SP shale baseline across the Mozumi fault may indicate a zone of enhanced permeability. The gamma ray log indicates areas of naturally occurring radioactivity, or shale content, in the Mozumi fault, as do spot core logs and physical core available for this study. The sonic log shows slower velocities for shale or siltstone within the Mozumi fault zone than shale or siltstone outside of the fault zone, indicating porosity has been created within the fault zone.

[24] The values of the shear wave and compression wave velocities are also slower across the Mozumi fault (1.99 ± 0.05 and 4.04 ± 0.06 km/s) relative to surrounding wall rock (2.36 ± 0.05 and 4.36 ± 0.08 km/s). A Mann-Whitney U test for comparison of two sample populations of nonparametric, open data was employed to test for statistical significance of the decrease in seismic velocity across the Mozumi fault zone. The null hypothesis of h1: velocities across the Mozumi fault zone $\geq$ velocities of wall rock was rejected at a confidence interval of 95%. Thus the decrease in seismic wave velocity across the Mozumi fault zone is statistically significant. This indicates that fault-related activity and perhaps the alteration discussed above has significantly altered the physical properties of the Mozumi fault rocks relative to wall rock.

3.2. Calculations of Elastic Moduli and Porosity

[25] We determine elastic modulii of rocks within the fault zone from seismic wave velocities recorded by wireline logs and the rock density. Density was measured for all

Table 2. Bulk and Clay Mineralogy by Sample

Sample	Bulk Mineralogy	Clay Mineralogy
MZA-2	quartz, feldspar, muscovite	smectite, illite, kaolinite, I-S chlorite
MZA-1	quartz, calcite, muscovite	illite, smectite, kaolinite
MZA-5	quartz, calcite, feldspar, muscovite	illite, kaolinite, chlorite or vermiculite, smectite?
MZA-6	quartz, calcite, muscovite	illite, smectite, kaolinite
MZA-7	quartz, feldspar, muscovite	illite, kaolinite
MZA-8	quartz, muscovite	illite, kaolinite
MZA-9a	quartz, calcite, muscovite	illite, kaolinite-smectite, chlorite or vermicullite
MZA-9b	quartz, calcite, muscovite	illite, kaolinite, chlorite
MZA-10	quartz, calcite, muscovite	illite, kaolinite, chlorite or vermicullite
MZ-1 MZ-1A	quartz, feldspar, muscovite	illite, kaolinite, I-S? no clays in 1A

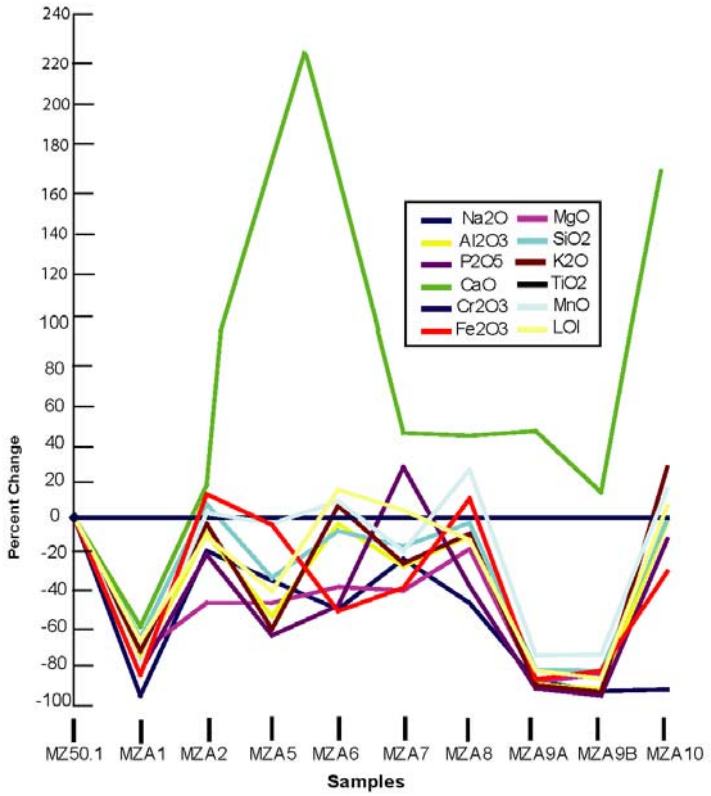

Figure 8. Percent changes in mobile oxides from siltstone protolith (MZ-1) in borehole 1 to fault zone rocks in borehole A of the Active Fault Survey Tunnel [*Goddard and Evans*, 1995]. Overall, fault zone rocks are depleted in mobile oxides relative to the protolith, with the exception of CaO. Samples MZA-1 and MZA-9 are most depleted and have undergone very significant chemical changes relative to the protolith.

samples collected from borehole A by simple displacement of water methods. The values of Lame's constant λ, and the shear modulus μ (a measure of rigidity) can be calculated from:

$$V_s = \sqrt{\mu/\rho} \tag{1}$$

and

$$V_p = \sqrt{(K + 4/3\mu)/\rho} = \sqrt{(\lambda + 2\mu)/\rho} \tag{2}$$

where V_s is shear wave velocity from the wireline log, V_p is the compressional wave velocity from the wireline log, K is the bulk modulus, μ is the shear modulus, and ρ is calculated density [*Kramer*, 1996]. Using λ and μ, Young's modulus (E) and Poisson's ratio (ν) can be calculated for borehole A samples using [*Kramer*, 1996; *Mavko et al.*, 1998]

$$E = (\mu(3\lambda + 2\mu))/(\lambda + \mu) \tag{3}$$

and

$$\nu = \lambda/2(\lambda + \mu) \tag{4}$$

Thus we estimate the elastic properties of fault zone materials, and use these values in conjunction with observations of fault rock properties to infer the physical properties of the fault zone (Table 3).

[26] Calculated values for Young's modulus and Poisson's ratio fall toward the high end or above experimentally derived values measured for intact samples of siltstone, shale, and sandstone (Figure 10) [*Haas*, 1981; *Szwilski*, 1982; *Hatheway and Kiersch*, 1989; *Wong et al.*, 1997]. Laboratory values for seismic velocities and elastic moduli are often different than in situ values due to biased sampling of unfractured, undeformed, pure rock samples for laboratory testing [*Stierman and Kovach*, 1979; *Sayed*, 2001]. This would result in faster seismic velocity, higher Young's modulus, and lower Poisson's ratio values for laboratory experiments with respect to in situ values. The Poisson's ratio determined here is indeed lower for experimentally derived values (average of 0.206) than values calculated from in situ seismic velocities of the Mozumi fault zone (average of 0.320; Figure 10). The value of Young's modulus, however, is higher in the naturally deformed rocks (average of 29.9 GPa) than for experimental values (average of 20.5 GPa). Values of Young's modulus may be higher for Mozumi fault zone siltstone than for laboratory samples of sandstone, shale, and siltstone due to cementation and mineralization as observed in thin section (Figure 6), or

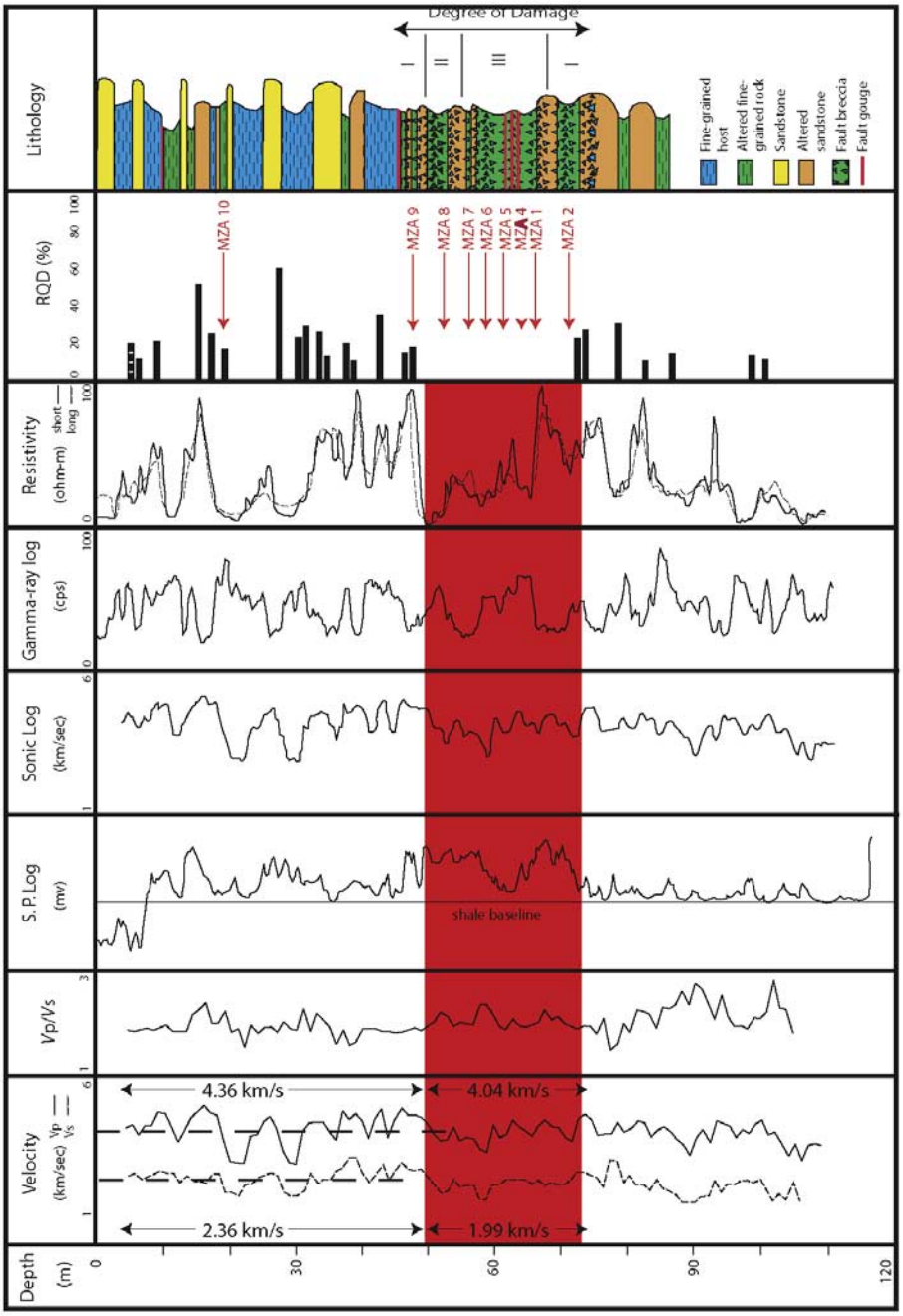

Figure 9. Wireline logs, sample positions, and correlated and interpreted lithology of borehole A [*Shingu et al.*, 1997].

due to the presence of interstitial (and incompressible) fluids in the fault [*Forster et al.*, 2003]. Mineralization may account for the stiffness of the fault rocks relative to pure sandstone and siltstone samples used in laboratory testing for Young's modulus.

[27] The amount of clay in each sample was determined with a hydrometer in the Utah State University Soil Testing Laboratory (Table 4). Some error is introduced as small (<mm) pieces of siltstone breccia clasts did not completely disaggregate upon mixing. The hydrometer measures the density of soil (clay) colloids. Once the clay content is estimated for each sample, we can calculate porosity (ϕ) from the velocity data by

$$V_p = 5.77 - 6.94\phi - 1.73\sqrt{C} + 0.446\left(P_e - 1.0e^{-16.7Pe}\right) \quad (5)$$

where C is the clay volume fraction and P_e is the effective pressure in kilobars (Table 4) [*Eberhart-Phillips et al.*, 1989]. The confining pressure at the tunnel depth of 350 m is 7.6 MPa [*Forster et al.*, 2003], and we assume a hydrostatic gradient for the fluid pressure. The confining pressures for core samples were calculated using the true

Table 3. Estimated Values for Properties of Mozumi Fault Rocks[a]

Sample	ρ (g/cm^3)	ν_s (km/s)	ν_p (km/s)	μ (g/cm s^2)	λ (g/cm s^2)	Calculated E (GPa)	Calculated ν	V_p/V_s	Calculated Porosity (%) (5), (6)	Permeability (m^2), Connected Porosity (%) of *Forster et al.* [2003]
MZA-2	2.77	2.20	4.16	1.34×10^{11}	2.11×10^{11}	35.0	0.306	1.89	10, 11	$3.7\ E^{-15}$, 8.0
MZA-1	2.49	2.13	3.76	1.13×10^{11}	1.26×10^{11}	28.6	0.264	1.77	17, 16	$1.9\ E^{-15}$, 8.4
MZA-4	2.33	2.25	4.31	1.18×10^{11}	1.97×10^{11}	31.0	0.263	1.92	-	$5.3\ E^{-15}$, 9.0
MZA-5	2.80	2.05	3.90	1.18×10^{11}	1.90×10^{11}	30.9	0.308	1.90	14, 14	$1.6\ E^{-15}$, 7.2
MZA-6	2.87	1.45	3.45	6.03×10^{10}	2.21×10^{11}	16.2	0.393	2.38	22, 20	
MZA-7	2.56	2.00	3.90	1.02×10^{11}	1.85×10^{11}	27.1	0.322	1.95	15, 15	
MZA-8	2.60	1.75	3.83	7.96×10^{10}	2.22×10^{11}	21.8	0.368	2.19	16, 16	
MZA-9a	2.66	2.55	4.76	1.73×10^{11}	2.57×10^{11}	44.9	0.299	1.87	-	
MZA-9b	2.41	2.55	4.76	1.57×10^{11}	2.32×10^{11}	40.8	0.298	1.87	-	
MZA-10	2.84	1.70	3.79	8.21×10^{10}	2.44×10^{11}	22.6	0.374	2.23	18, 17	
Borehole 1 Protolith										
MZ-1	2.85	2.80	4.75	2.23×10^{11}	2.10×10^{11}	55.4	0.242	1.70	4, 6	$4.0\ E^{-17}$, 1.6
MZ 1A	2.83	2.91	4.83	2.34×10^{11}	2.27×10^{11}	57.3	0.19	1.71	7	
Additional Samples From Forster et al. [2003]										
MZA-143.2 (breccia)										$3.7\ E^{-15}$, 8.0
MZA-127.8 (clay gouge)										$2.2\ E^{-16}$, 11.1
"Clay-rich zones"										$E^{-18} - E^{-19}$

[a]Properties include density (ρ), seismic wave velocities (V_s, V_p), calculated physical, and calculated mechanical properties for borehole A samples and a protolith sample from borehole 1, as well as permeability and porosity values from *Forster et al.* [2003].

depth below the ground surface for each sample. Calculated porosity values from equation (5) are similar to calculated porosity values using the following equation derived by *Castagna et al.* [1985]:

$$V_p = 5.81 - 9.42\phi - 2.21V_{cl} \quad (6)$$

where V_{cl} is the clay volume. Calculated porosity values are listed in Table 3. These relationships are derived from regressions of experimentally determined values of P_e is, ϕ, V_{cl}, V_p, and V_s. An RMS curve fit is applied to the data [*Eberhart-Phillips et al.*, 1989] so that a relationship between the velocities and physical properties is extracted.

[28] The V_p/V_s values (Table 3) are a proxy for fluid content and porosity, with high V_p/V_s values indicating an increased presence of fluids and porosity [*Stanchits et al.*, 2003]. Portions of the Mozumi fault zone have high relative fluid content (V_p/V_s = 2.19–2.38) (Table 3), whereas some portions of the fault zone have lower values of V_p/V_s (1.77–1.95) and higher S wave velocity values (2.00–2.55 km/s). Typical V_p/V_s values for sandstone, shale, and siltstone range from 1.5 (dry sandstone) to ~2.5 [*Castagna et al.*, 1985], and the velocity reduction calculated here for the fault zone is consistent with velocity reductions associated with clay and fluid content of rock [*Klimentos and McCann*, 1990; *Wang and Nur*, 1990].

[29] We compare our calculated values of Poisson's ratio from our data to compilations for unfaulted siltstone and sandstones by *Castagna et al.* [1985] and to the analysis of similar rocks by *Brocher* [2005] (Figure 11), in which Poisson's ratio is examined as a function of V_p. Most of the fault-related rocks examined here have values of ν that are higher than that of the global populations, and from (4), we infer that most of this increase is due to the decrease in μ, the shear modulus of the rocks. We suggest that the higher porosity in the damage zone [*Forster et al.*, 2003] and the fluid-rich clay alteration products documented here contribute to lower values of the shear modulus in parts of the fault zone, and thus lower values of V_s, while higher values of E are produced by the presence of pore fluids and/or cements.

4. Discussion

[30] *Mizuno et al.* [2004] analyzed the Mozumi fault zone-trapped waves produced from 9 earthquakes and recorded by a seismic array within the Active Fault Survey Tunnel to infer fault zone structure including total damage zone width, average S wave velocity, and wave attenuation. They estimate the width of the fault zone to be 160–400 m, which corresponds to the damage zone observed by mine geologists in the Active Fault Survey Tunnel of ~200 m across the entire fault zone. The average shear wave velocity from the trapped wave study were 2.9–3.1 km/s, or ~1.0 km/s faster than the average value determined from the wireline log for Mozumi fault zone rocks. The seismic wave attenuation (Qs) in the fault zone is 60–90, much lower than normal crustal Q values of ~160 [*Anderson and Hart*, 1978; *Udias*, 1999].

[31] When combined with the result of our study, we can delineate the internal physical structure of the fault zone, and determine the chemical and mechanical processes responsible for the changes observed. *Mamada et al.* [2004] and *Mizuno et al.* [2004] provide analyses of the Mozumi fault zone over scales of tens to hundreds of meters, whereas our data provide data at the centimeters to tens of meters scale. Their results indicate the fault zone is a region of lower V_p and V_s, with geometric complexities affecting the movement of the head waves. The V_p and V_s values we determined from borehole A decrease from sandstone to shale to clay (Table 5 and Figure 9) [*Shingu et al.*, 1997]. In addition, seismic velocity values are decreased

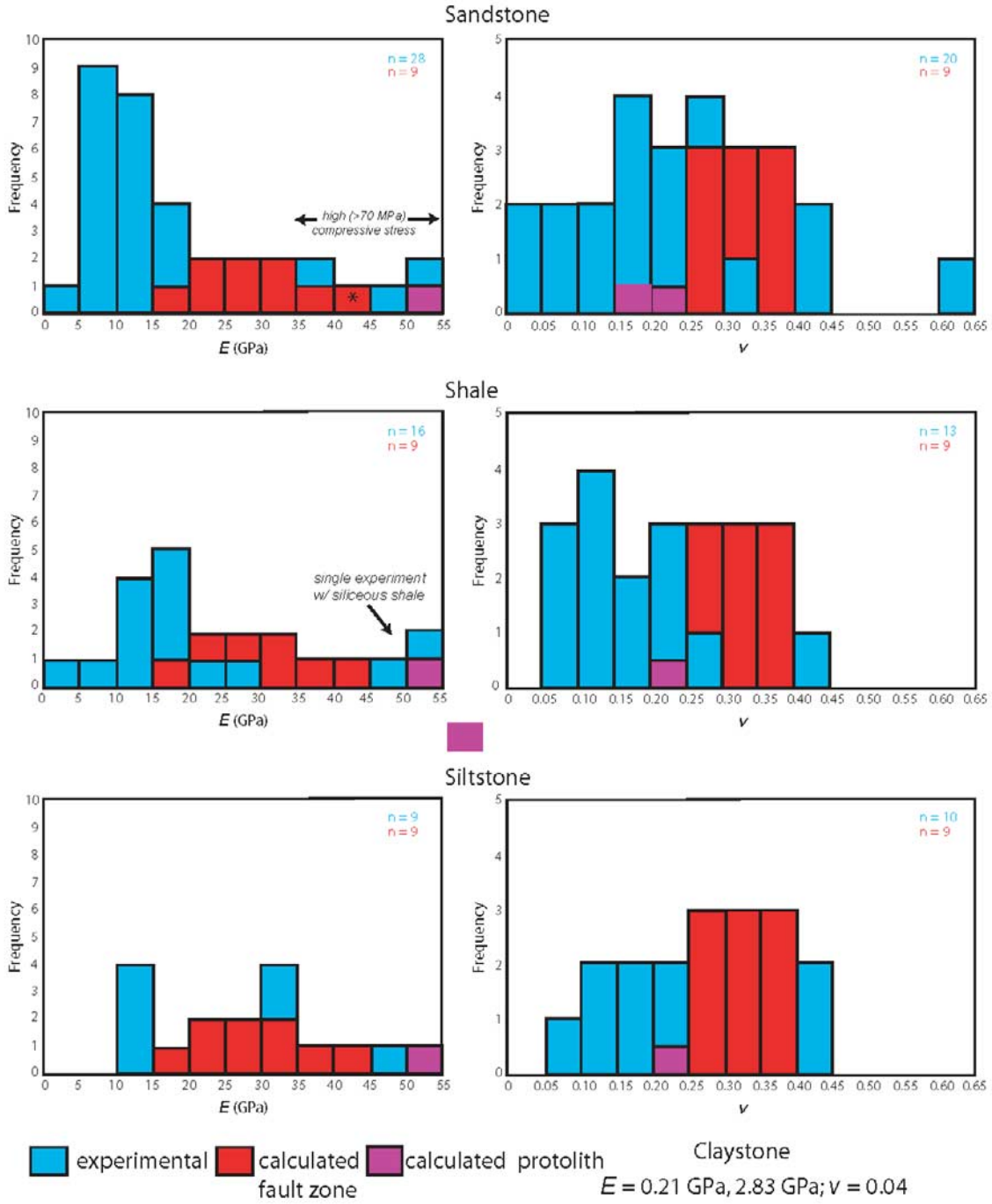

Figure 10. Histograms of the distribution of experimentally derived values for Young's modulus (E) and Poisson's ratio (v) for sandstone, shale, and siltstone, and calculated values for Mozumi fault rock samples. Data on claystone are very limited; thus values are simply listed. The calculated value for the protolith (samples MZ-1 and MZ-1A) of the Mozumi fault zone is indicated by the purple bar. The experimental data come from works referenced by *Haas* [1981]. Asterisk indicates complete overlap of blue and red bars.

across the Mozumi fault relative to the wall rock (Table 5 and Figure 9). The average P wave and S wave velocities determined from the seismic studies for protolith are 4.6–4.9 km/s and ~2.6–3.0 km/s, respectively [*Mamada et al.*, 2004; *Mizuno et al.*, 2004]. Four types of fault zone structures are recognized, including fractures along borehole A (Figure 6), lithology changes, including clay composition, foliation and other microstructures, and heterogeneity of physical and mechanical properties [*Forster et al.*, 2003; this study]. The wireline log data we present here (Figure 9)

Table 4. Hydrometer Results for Percent Clay Analysis

Sample	Sample Weight	40 s	Temp.	Corrected Hydrometer	6 h 40 s	Temp.	Corrected Hydrometer	Percentage Clay (±4%)
MZA-10	40	11.0	26	13.16	7.0	23	8.08	20
MZA-8	40	14.0	25	15.80	8.0	23	9.08	23
MZA-7	40	14.0	25	15.80	8.5	23	9.58	24
MZA-6	40	13.0	25	14.80	8.0	23	9.08	23
MZA-5	40	16.5	25	18.30	10.0	23	11.80	28
MZA-2	30	12.5	25	14.30	8.0	23	9.08	30
MZA-1	40	16.5	25	18.30	9.0	23	10.08	25
MZ-1	35	12.5	25	14.30	7.0	23	8.08	23
Control	40	3.0	26	5.16	3.0	23	4.08	14

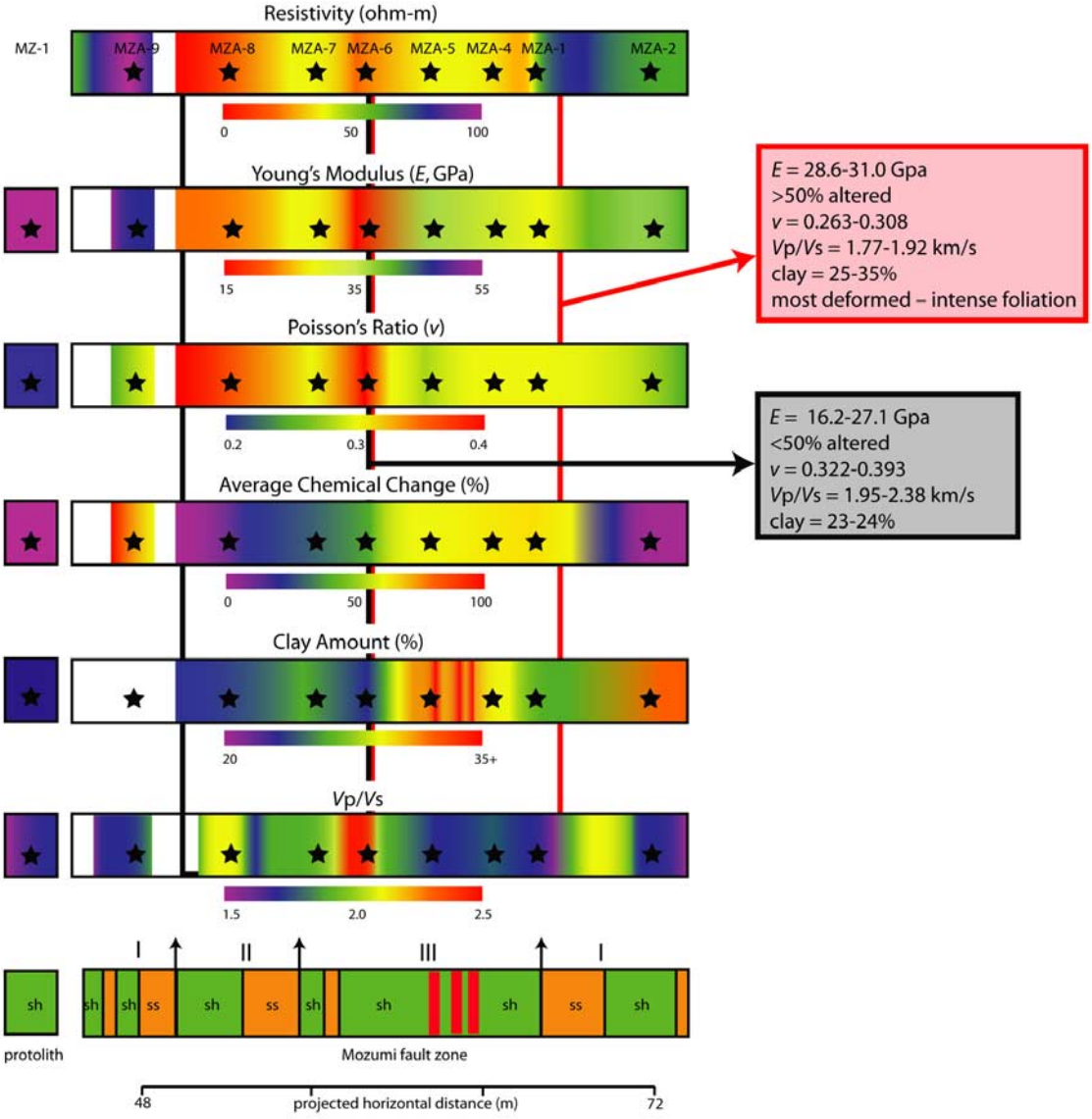

Figure 11. Representation of select properties across the Mozumi fault zone and properties of the protolith (MZ-1). Stars show the location of samples used in this study. General lithology is shown at the bottom of the page with sh, shale, and ss, sandstone. Red lines indicate the locations of clay gouge. Roman numerals indicate the degree of damage as assigned by mining geologists with I having the least damage and III having the most damage. The scales for each bar graph are based on typical maximums and minimums, as well as the range of values for Mozumi fault rocks [*Castagna et al.*, 1985], with the exception of clay amount, which is based on the values of Mozumi fault rocks and protolith so that the changes across the fault zone can be more easily observed.

Table 5. P Wave and S Wave Velocities for Borehole A by Rock Type, and Average P Wave Velocities for the Mozumi Fault Zone and Wall Rock[a]

	ν_p (km/s)		ν_s (km/s)	
Lithology	Range	Average	Range	Average
Sandstone	3.64–5.41	4.62	1.52–2.86	2.25
Mixed sandstone/shale	4.35–4.76	4.56	2.44–2.56	2.50
Shale	3.70–5.26	4.24	1.85–2.50	2.19
Siltstone	3.08–5.26	4.42	1.28–3.13	2.16
Clay	3.33–3.85	3.59	1.67–1.69	1.68
Average		4.49	average ν_p of MF zone	2.21
Average ν_p of wall rock		4.36	average ν_s of MF zone	4.04
Average ν_s of wall rock		2.36	typical range for ν_s	1.99
Typical range for ν_p		3.0–5.0		1.5–2.5

[a]Typical ranges of ν_p and νs for sandstones, shaley rocks, and "mudrocks" are listed [*Castagna et al.*, 1985].

suggest a slightly higher V_p and agree well with respect to V_s. The ~20% reduction of velocities are a result of both deformation and fluid-rock interactions.

[32] In detail, the relationships between geochemical, mineralogic, and physical properties of fault-related rocks are complex and variable across the fault zone. Portions of the fault zone are less dense, have low V_p/V_s values, low ν, and low resistivity values, have more clay content than other samples, and have the most depleted geochemical signatures. Interspersed with these deformed rocks are samples with high values of E (28.6 GPa and 31.0 GPa), low values of ν (0.264 and 0.263), and contain illite/muscovite and kaolinite clays. Low to intermediate fluid content (V_p/V_s = 1.87, 1.89, and 1.90), high values of E (40.8–44.9 GPa, 35.0 GPa, and 30.9), intermediate values of ν (0.298–0.299, 0.306), and mixtures of clay types also occur. Overall fluid-rock interactions, as depicted in the geochemical data, are also variable across the fault zone. These data illustrate the heterogeneous nature of the physical properties within the fault zone. Fault rocks of the Mozumi fault have values of Young's modulus ~11–39 GPa lower than the protolith samples, and values of Poisson's ratio 0.151–0.021 higher than protolith samples (Table 3). These values indicate that, overall, the fault zone rocks are not as stiff and have a greater porosity than their protolith.

[33] The abundance of veins throughout the Mozumi fault zone and numerous mineral phases present around the secondary fault indicate that fluid flow was active during and after fault motion. Veins that fill shattered grains indicate that fluids must have transported calcite and gouge into void spaces quickly before the fractures closed. Anastomosing gouge and irregular shaped blebs of coarse calcite crystals within the matrix indicate fluid pressurization and coseismic injection of fluids and saturated fault gouge. The available fluids that created these microstructures likely persisted after fault activity. Thin sections contain veins that show evidence for evolving fluids that precipitated quartz followed by calcite or chlorite.

[34] Permeability and porosity reported by *Forster et al.* [2003] indicate that permeability (k) and porosity (n) values in siltstone protolith is on the order of 10^{-17} m^2 and 1.6%, respectively, and that the smallest k values occur in clay-rich zones (10^{-18} to 10^{-19} m^2), with intermediate values of k and n in fault breccia with clay gouge (10^{-14} to 10^{-16} m^2, 8–9%) and the largest k values for fractured rock without significant clay content (10^{-13} to 10^{-14}, Table 3). The values of porosity calculated from clay content and wellbore based P wave velocity for fault rocks in this study are at least double the porosity values reported by *Forster et al.* [2003], whereas the values reported by *Forster et al.* [2003] measure connected porosity using the fluid injection method. Hydraulic conductivities determined from the in situ flow tests [*Nohara et al.*, 2006] reveal a lithology and structural dependence on hydraulic conductivity, with values ranging from 10^{-6} to 10^{-7} m/sec.

[35] Our data presented in this study, and recent work of others support an interpretation of the heterogeneous structure of the Mozumi fault [*Forster et al.*, 2003; *Nohara et al.*, 2006]. Permeable zones of brecciated fault rock correspond to areas of low relative resistivity, high relative values of V_p/V_s, low values of E, and high values of ν (Figure 11). Fault-related rocks with lower values of V_p/V_s correspond to a greater percentage of clay, higher resistivity values, are more chemically altered than protolith, and these rocks have higher values of E, and have lower values of ν than the zones of permeable fault rock (Figure 11). The presence of smectite (as well as the geochemical alterations) indicates fluid-rock interactions, as the protolith is illite-siltstone. These observations suggest that pockets of fluid-rich rock may migrate through time, thus resulting in illite-smectite reactions and other alteration along the fault zone. The migration of fluid and resulting alteration may cause a gradual change in the behavior of the fault and the properties of that rock mass over time.

[36] We suggest that our data support a model of a heterogeneous Mozumi fault zone with fault-parallel, fluid-rich zones that are mixed with clay-rich zones and subvertial slip zones. Similar complexity of borehole log signatures, composition, and physical properties has been noted in decollement faults associated with accrectionary prisms [*Shipley et al.*, 1997; *Tobin and Moore*, 1997] and in active strike-slip faults [*Gettemy et al.*, 2004]. In detail, faults in fine-grained sedimentary rocks appear to exhibit significant internal structural and compositional variability that is reflected at a variety of scales and in a variety of signatures.

5. Conclusions

[37] We provide microstructural, mineralogical, and geochemical data, and calculated values of elastic modulii for fault rock samples from the Mozumi fault, Japan, that can be combined to illustrate the in situ macroscopic hydromechanical structure of the fault. The results of this and related studies include:

[38] 1. The Mozumi fault-related rocks are altered and mineralized fault breccias with foliated sericite/muscovite-rich matrix that show evidence for concentrating shear and plastic deformation in the matrix. The Mozumi fault is a low-velocity zone relative to wall rock in borehole A and protolith as determined from wireline logs of P wave and S wave velocities across the fault zone and seismic wave velocities of protolith as reported by *Mizuno et al.* [2004, and references therein].

[39] 2. Fault rocks from the Mozumi fault zone have increased porosity (10–22%) relative to the protolith. Electrical and seismic properties, elastic moduli, porosity, permeability, fault-related textures, and clay content vary across the main fault zone. Rocks in which fluid-rock interactions were significant have low values of young's modulus and higher values of Poisson's ratio; fault breccias that have higher values of E, low to intermediate values of ν, and are more altered and contain more clay and intense microstructural deformation.

[40] 3. The attenuation factor Q, for the Mozumi fault zone is 60–90, whereas average crustal values are ~160 (*Mizuno et al.* [2004]; see also *Blakeslee et al.* [1989] for Q of faults). Combined with the microscturural and geochemical observations presented here, we suggest that these low Q values are a consequence of the accumulated effects of fault-related damage and fluid-rock alteration while the faults are active.

[41] **Acknowledgments.** We thank the staff of the AFST for access to the Mozumi tunnel and core from the site. This work was funded by a U.S. Geological Survey NEHRP grant to Evans and grants from DOSECC, the American Association of Petroleum Geologists, and the NSF–EAPSI program to Isaacs. Thorough reviews by Thomas Brocher and Yoshitaka Hashimoto greatly improved the paper.

References

Anderson, D. L., and R. S. Hart (1978), Attenuation models of the Earth, *Phys. Earth Planet. Inter.*, *16*, 289–306.

Ando, M. (1998), Overview and purpose of the active fault probe at the Mozumi-Atotsugawa fault system (progress report), in *The International Workshop of Frontiers in Monitoring Science and Technology for Earthquake Environments*, *Rep. TW7400 98-001*, Jpn. Nucl. Cycle Dev. Inst., Toki, Gifu, Japan, Nov.

Ben-Zion, Y. (1998), Properties of seismic fault zone waves and their utility for imaging low-velocity structures, *J. Geophys. Res.*, *103*, 12,567–12,585, doi:10.1029/98JB00768.

Ben-Zion, Y., and C. Sammis (2003), Characterization of fault zones, *Pure Appl. Geophys.*, *160*, 677–715, doi:10.1007/PL00012554.

Blakeslee, S., P. Malin, and M. Alvarez (1989), Fault-zone attenuation of high-frequency seismic waves, *Geophys. Res. Lett.*, *16*, 1321–1324, doi:10.1029/GL016i011p01321.

Brocher, T. M. (2005), Empirical relations between elastic wavespeeds and density in the Earth's crust, *Bull. Seismol. Soc. Am.*, *95*, 2081–2092, doi:10.1785/0120050077.

Caine, J. S., J. P. Evans, and C. B. Forster (1996), Fault zone architecture and permeability structure, *Geology*, *24*, 1025–1028, doi:10.1130/0091-7613(1996)024<1025:FZAAPS>2.3.CO;2.

Castagna, J. P., M. L. Batzle, and R. L. Eastwood (1985), Relationships between compressional-wave and shear-wave velocities in clastic silicate rocks, *Geophysics*, *50*, 571–581, doi:10.1190/1.1441933.

Chester, F. M., and J. M. Logan (1986), Implications for mechanical properties of brittle faults from observation of the Punchbowl fault zone, California, *Pure Appl. Geophys.*, *124*, 79–106, doi:10.1007/BF00875720.

Chester, F. M., J. P. Evans, and R. L. Biegel (1993), Internal structure and weakening mechanisms of the San Andreas fault, *J. Geophys. Res.*, *98*, 771–786.

Chester, F. M., J. M. Chester, D. L. Kirschner, S. E. Schulz, and J. P. Evans (2004), Structure of large-displacement, strike-slip fault zones in the brittle continental crust, in *Rheology and Deformation of the Lithosphere at Continental Margins*, edited by G. D. Karner et al., pp. 223–260, Columbia Univ. Press, New York.

Deere, D. U., and D. W. Deere (1987), The Rock Quality Designation (RQD) index in practice, *ASTM Spec. Tech. Publ.*, *984*, 91–101.

Eberhart-Phillips, D., and A. J. Michael (1998), Seismotectonics of the Loma Prieta, California, region determined from three-dimensional V_p, V_p/V_s, and seismicity, *J. Geophys. Res.*, *103*, 21,099–21,120, doi:10.1029/98JB01984.

Eberhart-Phillips, D. M., D.-H. Han, and M. D. Zoback (1989), Empirical relationships among seismic velocity, effective pressure, porosity, and clay content in sandstone, *Geophysics*, *54*, 82–89, doi:10.1190/1.1442580.

Erickson, S. G. (1994), Deformation of shale and dolomite in the Lewis thrust fault zone, northwestern Montana, U. S. A., *Can. J. Earth Sci.*, *31*, 1440–1448.

Evans, J. P., C. B. Forster, and J. V. Goddard (1997), Permeability of fault-related rocks, and implications for hydraulic structure of fault zones, *J. Struct. Geol.*, *19*, 1393–1404, doi:10.1016/S0191-8141(97)00057-6.

Faulkner, D. C., A. C. Lewis, and E. H. Rutter (2003), On the internal structure and mechanics of large strike-slip fault zones; field observations of the Carboneras fault in southeastern Spain, *Tectonophysics*, *367*, 235–251, doi:10.1016/S0040-1951(03)00134-3.

Forster, C. B., J. P. Evans, H. Tanaka, R. Jeffreys, and T. Nohara (2003), Hydrologic properties and structure of the Mozumi Fault, central Japan, *Geophys. Res. Lett.*, *30*(6), 8010, doi:10.1029/2002GL014904.

Fujita, M. (2002), A new contribution to the stratigraphy of the Tetori Group, adjacent to Lake Kuzuryu, Fukui Prefecture, central Japan, *Mem. Fukui Pref. Dinosaur Mus.*, *1*, 41–53.

Gettemy, G. L., H. J. Tobin, J. A. Hole, and A. Y. Sayed (2004), Multi-scale compressional wave velocity structure of the San Gregorio fault zone, *Geophys. Res. Lett.*, *31*, L06601, doi:10.1029/2003GL018826.

Goddard, J. V., and J. P. Evans (1995), Chemical changes and fluid-rock interaction in faults of crystalline thrust sheets, northwestern Wyoming, U. S. A., *J. Struct. Geol.*, *17*, 533–547, doi:10.1016/0191-8141(94)00068-B.

Haas, C. J. (1981), Static stress-strain relationships, in *Physical Properties of Rocks and Minerals*, edited by Y. S. Touloukian, W. R. Judd, and R. F. Roy, pp. 409–489, McGraw-Hill, New York.

Hardebeck, J. L., A. J. Michael, and T. M. Brocher (2007), Seismic velocity structure and seismotectonics of the eastern San Francisco bay region, California, *Bull. Seismol. Soc. Am.*, *97*(3), doi:10.1785/0120060032.

Hatheway, A. W., and G. A. Kiersch (1989), Engineering properties of rock, in *Practical Handbook of Physical Properties of Rocks and Minerals*, edited by R. S. Charmichael, pp. 672–715, CRC Press, Boca Raton, Fla.

Heermance, R. V., Z. K. Shipton, and J. P. Evans (2003), Fault structure control on fault slip and ground motion during the 1999 rupture of the Chelungpu fault, Taiwan, *Bull. Seismol. Soc. Am.*, *93*, 1034–1050, doi:10.1785/0120010230.

Hirahara, K., Y. Ooi, M. Ando, Y. Hoso, Y. Wada, and T. Ohkura (2003), Dense GPS array observations across the Atotsugawa fault, central Japan, *Geophys. Res. Lett.*, *30*(6), 8012, doi:10.1029/2002GL015035.

Holland, M., J. L. Urai, W. van der Zee, H. Stanjek, and J. Konstanty (2006), Fault gouge evolution in highly overconsolidated claystones, *J. Struct. Geol.*, *28*, 323–332, doi:10.1016/j.jsg.2005.10.005.

Ito, H. (1999), Studies on fault activity at the Atotsugawa fault—Is the Atotsugawa fault creeping?, *Geol. Surv. Jpn. Inf. Circ.*, *S-12*.

Ito, H. (2003), Detailed seismicity and crustal structure in the Atotsugawa fault, a partly creeping fault, central Honshu, Japan, paper presented at 2003 Scientific Program, Int. Union of Geod. and Geophys., Sapporo, Japan, 30 June to 11 July.

Kawai, M., and T. Nozawa (1958), Explanatory text of the geological map of Japan, Kanazawa-36 region, scale 1:50,000, 76 pp., Geol. Surv. of Jpn., Tsukuba.

Keller, J. V. A., S. H. Hall, C. J. Dart, and K. R. McClay (1995), The geometry and evolution of a transpressional strike-slip system: The Carboneras fault, SE Spain, *J. Geol. Soc.*, *152*, 339–351, doi:10.1144/gsjgs.152.2.0339.

Klimentos, T., and C. McCann (1990), Relationships among compressional wave attenuation, porosity, clay content, and permeability in sandstones, *Geophysics*, *55*, 998–1014, doi:10.1190/1.1442928.

Kramer, S. L. (1996), Earthquakes and wave propagation, in *Geotechnical Earthquake Engineering*, pp. 18–53 and 143–183, Prentice-Hall, Upper Saddle River, N. J.

Li, Y. G., and J. E. Vidale (1996), Low-velocity fault-zone guided waves: Numerical Investigations of trapping efficiency, *Bull. Seismol. Soc. Am.*, *86*, 371–378.

Li, Y. G., K. Aki, J. E. Vidale, and F. Xu (1999), Shallow structure of the Landers fault zone from explosion-generated trapped waves, *J. Geophys. Res.*, *104*, 20,257–20,275, doi:10.1029/1999JB900194.

Li, Y., J. E. Vidale, D. D. Oglesby, S. M. Day, and E. Cochran (2003), Multiple-fault rupture of the *M*7.1 Hector Mine, California, earthquake from fault zone trapped waves, *J. Geophys. Res.*, *108*(B3), 2165, doi:10.1029/2001JB001456.

Li, Y. G., J. E. Vidale, and E. S. Cochran (2004), Low-velocity damaged structure of the San Andreas fault at Parkfield from fault zone trapped waves, *Geophys. Res. Lett.*, *31*, L12S06, doi:10.1029/2003GL019044.

Mamada, Y., Y. Kuwahara, H. Ito, and H. Takenaka (2002), 3-D finite-difference simulation of seismic fault zone waves, Application to the fault zone structure of the Mozumi-Sokenobu fault, central Japan, *Earth Planets Space*, *54*, 1055–1058.

Mamada, Y., Y. Kuwahara, H. Ito, and H. Takenaka (2004), Discontinuity of the Mozumi–Sukenobu fault low-velocity zone, central Japan, inferred from 3-D finite-difference simulation of fault zone waves excited by explosive sources, *Tectonophysics*, *378*, 209–222, doi:10.1016/j.tecto.2003.09.008.

Mariko, T., M. Kawada, M. Miura, and S. Ono (1996), Ore formation processes of the Mozumi skarn-type Pb-Zn-Ag deposits in the Kamioka Mine, Gifu Prefecture, central Japan; a mineral chemistry and fluid inclusion study, *Resour. Geol.*, *46*, 337–354.

Matsuda, T. (1966), Strike-slip faulting along the Atotsugawa fault, Japan (in Japanese with English summary), *Bull. Earthquake Res. Inst. Univ. Tokyo*, *44*, 1179–1212.

Mavko, G., M. Tapan, and J. Dvorkin (1998), *The Rock Physics Handbook: Tools for Seismic Analysis in Porous Media*, 329 pp., Cambridge Univ. Press, Cambridge, U. K.

McGuire, J., and Y. Ben-Zion (2005), High-resolution imaging of the Bear Valley section of the San Andreas fault at seismogenic depths with fault-zone head waves and relocated seismicity, *Geophys. J. Int.*, *163*, 152–164, doi:10.1111/j.1365-246X.2005.02703.x.

Mikumo, T., H. Wada, and M. Koizumi (1988), Seismotectonics of the Hida region, central Honshu, Japan, *Tectonophysics*, *147*, 95–119, doi:10.1016/0040-1951(88)90150-3.

Mizuno, T., K. Nishigama, H. Ito, and Y. Kuwahara (2004), Deep structure of the Mozumi-Sukenobu fault, central Japan, estimated from the subsurface array observation of fault zone trapped waves, *Geophys. J. Int.*, *159*, 622–642, doi:10.1111/j.1365-246X.2004.02458.x.

Nohara, T., H. Tanaka, K. Watanabe, N. Furukawa, and A. Takami (2006), In situ hydraulic tests in the active fault survey tunnel, Kamioka Mine, excavated through the active Mozumi-Sukenobu Fault zone and their hydrogeological significance, *Isl. Arc*, *15*, 537–545, doi:10.1111/j.1440-1738.2006.00548.x.

Rutter, E. H., R. H. Maddock, S. H. Hall, and S. H. White (1986), Comparative microstructures of natural and experimentally produced clay-bearing fault gouges, *Pure Appl. Geophys.*, *124*, 3–30, doi:10.1007/BF00875717.

Sayed, A. Y. (2001), In Situ compressional wave velocity across an exposed brittle fault zone, Master's thesis, 40 pp., Polytech. Inst. and State Univ., Blacksburg, Va.

Schulz, S. E., and J. P. Evans (2000), Mesoscopic structure of the Punchbowl fault, southern California, and the geologic and geophysical structure of active strike-slip faults, *J. Struct. Geol.*, *22*, 913–930, doi:10.1016/S0191-8141(00)00019-5.

Shingu, K., T. Okada, A. Saitou, K. Wada, K. Horinokuchi, and T. Nakajima (1997), Study using a drift in the active fault zone (in Japanese with English abstract), *Rep. TJ1174 97-001*, Power Reactor and Nucl. Fuel Dev. Corp., Gifu, Japan.

Shipley, T. H., G. F. Moore, J. J. Tobin, and J. C. Moore (1997), Synthesis of the Barbados decollement seismic reflection response from drilling-based geophysical observations and physical properties, *Proc. Ocean Drill. Program Sci. Results*, *156*, 293–302.

Spudich, P., and K. B. Olsen (2001), Fault zone amplified waves as a possible seismic hazard along the Calaveras fault in central California, *Geophys. Res. Lett.*, *28*, 2533–2536, doi:10.1029/2000GL011902.

Stanchits, S. A., D. A. Lockner, and A. V. Ponomarev (2003), Anisotropic changes in P wave velocity and attenuation during deformation and fluid infiltration of granite, *Bull. Seismol. Soc. Am.*, *93*, 1803–1822, doi:10.1785/0120020101.

Stierman, D. J., and R. L. Kovach (1979), An in situ velocity study: The Stone Canyon Well, *J. Geophys. Res.*, *84*, 672–678, doi:10.1029/JB084iB02p00672.

Szwilski, A. B. (1982), Determination of elastic modulus of stress relief cores of shale, *Geotech. Test. J.*, *5*, 34–41.

Takeuchi, A., H. Ongirad, and T. Akimitsu (2003), Recurrence interval of big earthquakes along the Atotsugawa fault system, central Japan: Results of seismo-geological survey, *Geophys. Res. Lett.*, *30*(6), 8011, doi:10.1029/2002GL014957.

Thurber, C., H. Zhang, F. Waldhauser, J. Hardebeck, A. Michael, and D. Eberhart-Phillips (2006), Three-dimensional compressional wavespeed model, earthquake relocations, and focal mechanisms for the Parkfield, California, region, *Bull. Seismol. Soc. Am.*, *96*(4B), S38–S49, doi:10.1785/0120050825.

Tobin, H. J., and J. C. Moore (1997), Variations in ultrasonic velocity and density with pore press in the decollement zone, northern Barbados ridge accretionary prism, *Proc. Ocean Drill. Program Sci. Results*, *156*, 125–135.

Udias, A. (1999), Anelasticity and anisotropy, in *Principles of Seismology*, pp. 253–273, Cambridge Univ. Press, Cambridge, U. K.

Wada, H., T. Mikumo, and M. Koizumi (1990), Recent seismic activity in the northern Hida, Toyama Bay and Noto Peninsula regions, Kyoto Daigaku Bosai Kenkyujo Nenpo, *Ann. Disaster Prev. Res. Inst.*, *33*, 57–74.

Wang, Z., and A. Nur (1990), Wave velocities in hydrocarbon-saturated rocks: Experimental results, *Geophysics*, *55*, 723–733, doi:10.1190/1.1442884.

Warr, L. N., and S. Cox (2001), Clay mineral transformation and weakening mechanisms along the Alpine fault, New Zealand, in *The Nature And Tectonic Significance of Fault Zone Weakening*, edited by R. E. Holdsworth et al., *Geol. Soc. Spec. Publ.*, *186*, 103–112.

Wibberley, C. A. J., and T. Shimamoto (2003), Internal structure and permeability of major strike-slip fault zones: The Median Tectonic line in Mie Prefecture, southwestern Japan, *J. Struct. Geol.*, *25*, 59–78, doi:10.1016/S0191-8141(02)00014-7.

Wong, T., C. David, and W. Zhu (1997), The transition from brittle faulting to cataclastic flow in porous sandstones: Mechanical deformation, *J. Geophys. Res.*, *102*, 3009–3025, doi:10.1029/96JB03281.

Yamada, K., S. Niwa, and M. Kamata (1989), Lithostratigraphy of the Mesozoic Tetori Group in the upper reaches of the Kuzuryu River, Japan, *J. Geol. Soc. Jpn.*, *95*, 391–403.

Yan, Y., B. A. van der Pluijm, and D. R. Peacor (2001), Deformation microfabrics of clay gouge, Lewis Thrust, Canada: A case for fault weakening from clay transforation, in *The Nature And Tectonic Significance of Fault Zone Weakening*, edited by R. E. Holdsworth et al., *Geol. Soc. Spec. Publ.*, *186*, 112–124.

J. P. Evans and P. T. Kolesar, Department of Geology, Utah State University, 4505 Old Main Hill, Logan, UT 84322-4505, USA. (jpevans@cc.usu.edu)

A. J. Isaacs, Anadarko Petroleum Corporation, 1099 18th Street, Suite 1200, Denver, CO 80202, USA.

T. Nohara, Geological Isolation Research Project, Neotectonics Research Group, Japan Atomic Energy Agency, 959-31, Toki, Gifu 509-5102, Japan.